Fluctuation-based fracture mechanics of heterogeneous materials

T. Mulla,[1] R. J.-M. Pellenq,[1,2,3] and F.-J. Ulm[1,2]

[1]*Department of Civil and Environmental Engineering, Massachusetts Institute of Technology, Cambridge, Massachusetts 02139, USA*
[2]*MIT-CNRS-AMU Joint Laboratory, Massachusetts Institute of Technology, Cambridge, Massachusetts 02139, USA*
[3]*Department of Physics, Georgetown University, Washington, DC, USA*

(Received 19 April 2021; accepted 27 November 2022; published 22 December 2022)

We present results of a hybrid analytical-simulation investigation of the fracture resistance of heterogeneous materials. We show that bond-energy fluctuations sampled by Monte Carlo simulations in the semigrand canonical ensemble provide a means to rationalize the complexity of heterogeneous fracture processes, encompassing probability and percolation theories of fracture. For a number of random and textured model materials, we derive upper and lower bounds of fracture resistance and link bond fracture fluctuations to statistical descriptors of heterogeneity, such as two-point correlation functions, to identify the origin of toughening mechanisms. This includes a shift from short- to long-range interactions of bond fracture processes in random systems to the transition from critical to subcritical bond fracture percolation in textured materials and the activation of toughness reserves at compliant interfaces. Induced by elastic mismatch, they connect to a number of disparate experimental observations, including toughening of brittle solids by deformable polymers or organics in, e.g., gas shale, nacre; stress-induced transformational toughening in ceramics; and toughening of sparse elastic networks in hydrogels, to name a few.

DOI: 10.1103/PhysRevE.106.065003

I. INTRODUCTION

Fracture of heterogeneous materials remains an important topic amid the backdrop of an ever-increasing demand for new materials specifically designed to overcome intrinsic trade-offs between competing material properties within composites [1–3], porous media [4,5], additively manufactured materials [6–8], and biological or bioinspired tissues [9–12]. However, this ever-expanding roster of heterogeneous materials has yet to find a consolidating theory of fracture mechanics, which bridges between two apparently disparate lines of advanced theories. On the one hand, early approaches based on Griffith's energy release rate [13,14] and Irwin's stress intensity factor [15,16] provide useful insights into benchmark phenomena in fracture of textured matrix-inclusion composites, such as crack trapping or bridging by arrays of obstacles (e.g., particles) [17–20], crack deflection, shielding or penetration at interfaces of dissimilar solids [21–23], and so on. These principles continue to reverberate in the contemporary computational fracture mechanics of multiscale composites (see, for instance, [24–26]) and composite material design [27–30]. On the other hand, statistical models of fracture in disordered materials have been derived from extreme value theory [31–33] and applied to random fiber-bundle [34] and lattice models [35–37], including their electric analogs, random fuse networks [38]. Moreover, these statistical models are capable of modeling heterogeneity by presenting an initial disorder in or random field of fracture strength or fracture strain threshold. Motivated by the intimate interplay of disorder and long-range correlations in fracture [39], such statistical physics approaches point to a number of intriguing features of fracture of heterogeneous materials, ranging from universality and scale invariance of the crack morphology or roughness [40–44], to power-law percolation behavior due to disorder in heterogeneous materials [45–48] and dynamical order parameters associated with crack front propagation [49–52].

Many models for effective fracture toughness can be found in the literature of statistical physics and thermodynamics that focus on (1) collective versus independent pinning in function of material disorder [53], (2) long- versus short-range interactions [54], (3) heterogeneity characterization by two-point correlation functions [55–57], (4) extracting fracture resistance information from fracture surfaces [58], and (5) various homogenization schemes for effective fracture toughness of heterogeneous media [25,59]. An ideal framework to tackle the problem of fracture toughness of heterogeneous media must at least combine all these different observations in agreement with literature. Next, we propose such a method.

Herein we approach fracture of heterogeneous materials through a combination of two schools of thought. On the one side, we preserve the classical equilibrium-based Griffith-type fracture approach in form of an energy release criterion of bond fracture. On the other, we follow the statistical physics approach by considering the overriding strength of bond-energy fluctuations in the very definition of Griffith's energy release rate and fracture energy dissipation. Specifically, the fluctuations of interest will be that of bond number and bond energy, measured as covariances. Herein we discuss the application and analysis of this method to brittle fracture. By applying this synergistic approach to a suite of two- and three-dimensional (2D, 3D) multiphase sample materials, which range from textured to random heterogeneous model materials

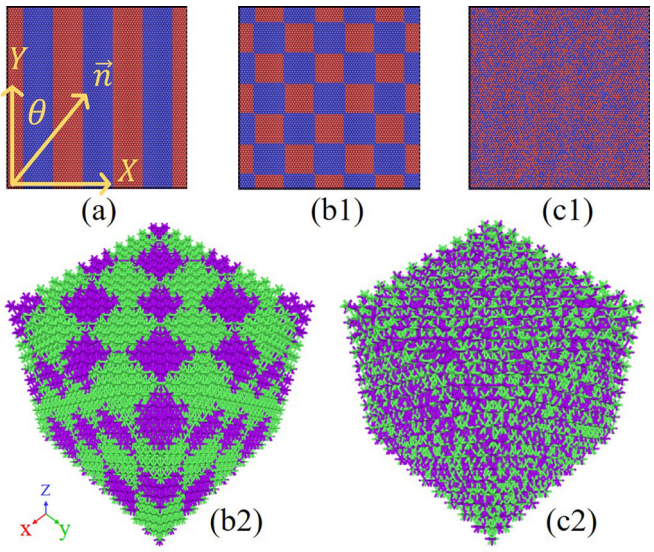

FIG. 1. Geometrically ordered and disordered two-phase materials: (a) layered material with inclined uniaxial stretch direction; (b1, b2) 2D and 3D checkerboard; and (c1, c2) 2D and 3D random material (visualized at $f_B = 50\%$).

(Fig. 1), we show that fluctuation-based fracture mechanics provides a means to derive the effective fracture resistance of heterogeneous materials, including upper and lower bounds and percolation thresholds.

For this investigation we carry out bond-centric Monte Carlo simulations in the semigrand canonical ensemble. More specifically, we impose a bond potential $\Delta\mu$, volume V, and temperature T, and perform bond-swapping trial moves in a $\Delta\mu VT$ ensemble and canonical displacement moves using molecular dynamics (MD) time integration in an NVT ensemble.

In the semigrand canonical Monte Carlo (SGCMC) approach, bonds N are switched "on" ($N \to N+1$) or "off" ($N \to N-1$), where N is the number of "on" (or unbroken) bonds, according to the following acceptance criterion:

$$\mathrm{acc}(o^* \to n^*) = \min(1, p_{o^* \to n^*}), \tag{1}$$

with

$$p_{N \to N+1} = \exp\left[\frac{1}{k_B T}(+\Delta\mu - \Delta U_{N \to N+1})\right], \tag{2}$$

$$p_{N \to N-1} = \exp\left[\frac{1}{k_B T}(-\Delta\mu - \Delta U_{N \to N-1})\right], \tag{3}$$

with $U_{o^* \to n^*} = U_{n^*} - U_{o^*}$ the difference in energy, $U = U^0 + U^\lambda$ (= ground-state + stretch energy, respectively), of microstates, $\mathcal{M}(o^*, n^*)$. The Monte Carlo (MC) simulations are considered converged if the probability of bond insertion and bond deletion are equal over a sufficiently large number of MC steps (i.e., the variances of N and of U converge to constant values). Moreover, probing bonds in this way in the MC simulations precludes the need for an *a priori* crack or notch in the system. In light of previous literature, if each bond is considered as an inclusion, the MC simulation starts out by probing individual bonds, and as accepted moves accrue, a collective behavior is manifested as a crack [54]. Otherwise stated, trial moves are attempted globally but are collectively accepted locally to give rise to a crack from a series of bond breaking events [53].

A. Heat of bond rupture

A key concept from the statistical physics of adsorption combined with knowledge of classical Griffith fracture mechanics paves the way for the introduction of a fluctuation-based fracture mechanics framework. At its core is the analogy between two derivatives and their immediate implication. We begin with the energy release rate [15,16,60]:

$$\mathcal{G} = -\frac{\partial E_{pot}}{\partial \Gamma}, \tag{4}$$

where E_{pot} is the potential energy and Γ is the fracture surface, readily understood over the past few decades as the change in energy (release) associated with change in fracture surface area [13,14,60]. Yet the crack or the fracture surface area are not in play for most of the fracture process, and if they are, they are static (in the case of stable crack propagation); they are more the aftermath of fracture. In contrast, for example, the bonds in a system holding the material together exist before fracture, and when a sufficient number of bonds break a crack or fracture, surface area is created. We thus move our frame of reference from the fracture surface area to it its precursor, the bonds in a bonded system. Keeping with the formulation of the energy release rate, we seek a derivative that describes the change in energy U with respect to change in bond number N. This derivative is the heat of bond rupture [61], adapted from the isosteric heats in the statistical physics of adsorption [62,63]:

$$q = -\frac{d\langle U\rangle}{d\langle N\rangle}. \tag{5}$$

This is the starting point for defining a fracture resistance in our fluctuation-based fracture mechanics approach [61], which we will explore further in the context of fracture of heterogeneous materials under quasistatic displacement-controlled loading.

II. PARTICIPANT VOLUME FRACTION

We probe all bonds in the system in the $\Delta\mu VT$ ensemble by sampling from an ensemble of equilibrated states. In the $\Delta\mu VT$ ensemble, we evaluate Griffith's energy release criterion for bond fracture from fluctuations of the bond energy of unbroken bonds, $N = N_0 - N_{br}$ (= total − broken number of bonds, respectively), by means of the heat of bond rupture, $q = q^0 + q^\lambda$, at the fracture phase transition [61,64,65]:

$$\frac{\mathrm{Cov}(U^\lambda, N)}{\mathrm{Cov}(N, N)} = -q^\lambda \equiv q^0 = -\frac{\mathrm{Cov}(U^0, N)}{\mathrm{Cov}(N, N)}. \tag{6}$$

Herein, $-q^\lambda$ stands for the bond-energy release rate due to bond stretching, U^λ. The link between Griffith's energy release criterion and the heats of bond rupture comes from the link between crack area and bond number. When a crack forms in a bonded system, bonds must necessarily break. As the energy release rate is a rate in terms of crack area change, the heats of bond rupture provide rates in terms of

bond number change. True to Griffith's fracture theory, this strain energy release rate equals the heat of bond rupture q^0 at fracture: it is the energy dissipated into heat by bond fracture and release of ground-state energy, $U^0 = -\mathbf{E^0} \cdot \mathbf{N}$, associated with bond numbers $\mathbf{N} = (N_A, N_B, \ldots, N_n)^T$:

$$q^0 = \mathbf{E^0} \cdot \frac{\mathrm{Cov}(\mathbf{N}, \mathbf{N})}{\mathrm{Cov}(N, N)} \cdot \mathbf{1}_{n,1} = \mathbf{E^0} \cdot \mathbf{S}, \tag{7}$$

with $\mathbf{E^0} = (\epsilon_A^0, \epsilon_B^0, \ldots, \epsilon_n^0)$ the vector of ground-state energies and $\mathbf{1}_{n,1}$ the vector of ones (noting that $N = \mathbf{1}_{1,n} \cdot \mathbf{N}$). Here we define a new quantity $\mathbf{S} = \frac{\mathrm{Cov}(\mathbf{N},\mathbf{N})}{\mathrm{Cov}(N,N)} \cdot \mathbf{1}_{n,1}$, termed the participant volume fraction and coined as such because it is a measure of the amount of each phase that participates in fracture (i.e., breaks); otherwise stated, $\mathbf{S}$ is the vector of "broken" bond fractions as opposed to the vector of "intact" bond fractions $\mathbf{f}$. In effect, Eq. (7) defines a homogenization scheme for fracture properties distinct from previous literature [25,59], where the focus in our SGCMC approach is shifted to the bond fractions of broken material. In terms of Griffith's coining, q^0 can be viewed as the bond fracture energy of the n-phase heterogeneous material. In return, enabled by the semigrand canonical sampling, the bond fraction of each phase participating in the fracture process, $\mathbf{S} = (S_\alpha, S_\beta, \ldots S_n)^T$, permits a dual definition from both fluctuation and probability theories. [In labeling intact and broken bonds in different phases, uppercase English letters $(A, B, \ldots)$ are reserved for intact bonds, and lowercase Greek letters $(\alpha, \beta, \ldots)$ are reserved for broken bonds.] Viewing S_β as the probability of a phase B bond breaking at fracture (which is the intersection of two events: being a phase B bond and being broken),

$$0 \leqslant S_\beta = \sum_{i=1}^{n} \frac{\mathrm{Cov}(N_i, N_B)}{\mathrm{Cov}(N, N)} \equiv \sum_{i=1}^{n} P(\beta \cap f_i) \leqslant 1 \tag{8}$$

for all $S_i \in \mathcal{S} = \{S_i \mid \sum_{(n)} S_i = 1\} \subseteq \mathcal{F} = \{f_i \mid \sum_{(n)} f_i = 1\}$. Herein, $\beta = N_{br}^B / \langle N_{br} \rangle$ stands for the random vector of bonds in phase-B breaking at a probability $S_\beta = P(\beta)$. This probability, $P(\beta) = \mathrm{E}[\beta]$, is the sum of the joint probabilities $P(\beta \cap f_i) = P(f_i)P(\beta \mid f_i)$, with $f_i = P(f_i) \sim N_{i,0}/N_0$ the volume fraction of each phase, and $P(\beta \mid f_i)$ the conditional probability. The synergy of the dual definition from Eq. (8) is recognized in the determination of bounds of the "effective" fracture resistance among all uncorrelated [i.e., $\mathrm{Cov}(N_{i\neq B}, N_B) = 0$] *and* independent [i.e., $P(\beta \cap f_{i\neq B}) = P(\beta)P(f_{i\neq B})$] fracture events in the n phases. In the limit case of no correlation, $S_\beta^{\lim} = (\sigma_{N_B}/\sigma_N)^2 \equiv P(\beta \cap f_B)$, the bond fractions $S_i \in \mathcal{S}$ are the eigenvalues of the (diagonal) bond covariance matrix. Moreover, the lower and upper bounds [LB and UB, respectively, in Figs. 2(a) and 4(a,b)] are defined by the min-max values of a conditional probability, $0 \leqslant P(\beta \mid f_\beta) \leqslant 1$. Combining Eqs. (7) and (8), the bounds can be expressed as

$$\inf_{S_i \in \mathcal{S}, \mathbf{S}\cdot\mathbf{S}=1} (\mathbf{E^0} \cdot \mathbf{S}) \leqslant q^0 \leqslant \sup_{S_i \in \mathcal{S}, \mathbf{S}\cdot\mathbf{f}=\|\mathbf{S}\|^2} (\mathbf{E^0} \cdot \mathbf{S}), \tag{9}$$

where $\mathbf{f} = (f_A, f_B, \ldots, f_n)^T$ is the vector of volume fractions of the phases. These bounds include the case of equiprobable fracture events in the n phases $[P(\beta \mid f_B) = 1/n]$, which entails the arithmetic mean as effective fracture resistance, $q^{0,\mathrm{Hill}} = \mathbf{E^0} \cdot \mathbf{f}/n$, reminiscent of the Hill bound.

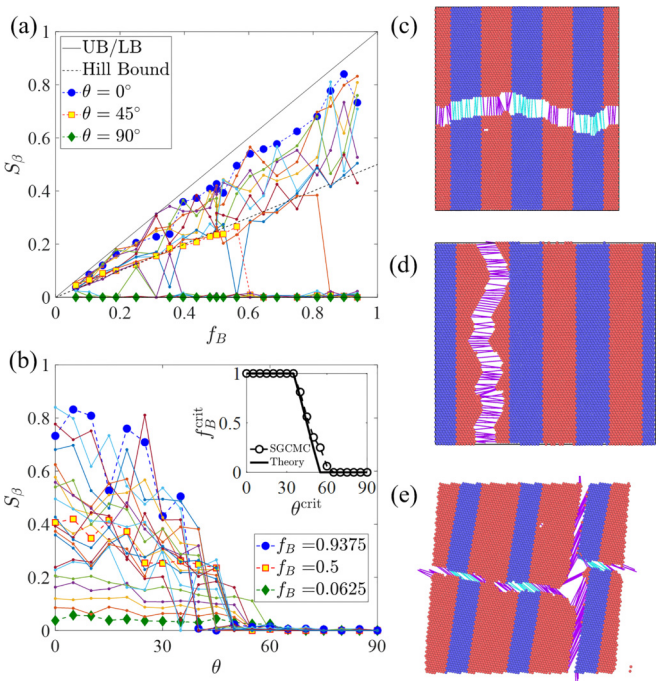

FIG. 2. Fracture of two-phase layered material under uniaxial stretching for different loading orientation angles: fraction of broken bonds that are phase B bonds, $S_\beta(f_B, \theta)$, as measured by Eq. (20) as function of (a) phase B bond fraction f_B, (direction of increasing θ is clockwise) and (b) loading angle θ (direction of increasing f_B is clockwise), with critical state line (inset); and bond fracture patterns: (c) upper bound ($\theta = 0$), (d) lower bound ($\theta = \pi/2$), (e) Hill bound at ($\theta = \pi/4$). For clarity only (a) 0°, 45°, and 90° loading angles and (b) representative volume fractions are labeled. Intermediate lines in (a) span 5° increments from 0° to 45° (inclusive), whereas all loading angles greater than 45° collapse to the lower bound (x axis: horizontal thin black line). Due to the resolution of the mesh, the increments in volume fraction in (b) are not equal; the labeled lines serve as guide markers.

The critical bond-energy release is the energy released by the removal of one (more) bond in a specific phase, when $q^0 = -q^\lambda$. In the SGC ensemble, this state is uniquely defined for a given volume, bond potential, and temperature along a critical line in the phase diagram of brittle fracture [61] and does not depend on the path to how this state is reached. We can thus define an expected value of q^0 from the sampled "space" average (ergodic theorem):

$$\mathrm{E}[q^0] = \frac{1}{\langle N_{br} \rangle} \int q^0 dN_{br} = \sum_{(n)} \epsilon_i^0 \frac{\langle N_{i,br} \rangle}{\langle N_{br} \rangle}, \tag{10}$$

where $\langle N_{i,br} \rangle$ and $\langle N_{br} \rangle$ stand for the ensemble average of *broken* bonds of phase $i = A, B, \ldots, n$ and all bonds, respectively. We can thus define the bond fraction participating in the fracture purely based on the bond fraction,

$$S_\beta = \mathrm{E}[\beta] = P(\beta) \quad \beta = \frac{N_{B,br}}{\langle N_{br} \rangle}. \tag{11}$$

Otherwise said, from a probability theory point of view, S_β represents the expected value of the bond fraction β of phase B participating in the fracture process. In return, this

probabilistic definition provides a dual definition based on the law of total probability:

$$P(\beta) = \sum_{i=1}^{n} P(\beta \cap f_i) = \sum_{i=1}^{n} P(\beta \mid f_i) P(f_i). \tag{12}$$

Equations (8) and (11) are two independent definitions of the participating bond fraction, S_β. In fact, the bond-fluctuation-based definition, Eq. (8), defines *correlatedness* between random variables $N_A, N_B, \ldots, N_n$ and obeys symmetry due to the symmetry of the covariance matrix, i.e., $\mathrm{Cov}(N_i, N_j) = \mathrm{Cov}(N_j, N_i)$. In contrast, the probability-based definition (12) defines dependence or independence of fracture events between these random variables, exhibiting no symmetry *a priori,* $P(\alpha \cap f_\beta) \neq P(\beta \cap f_\alpha)$. The two attributes, correlatedness *and* dependence, need to be independently evaluated for each specific situation.

III. METHODS

The backbone of our analysis is fracture mechanics in the semigrand canonical ensemble, $\Delta\mu VT$ ensemble. Recently proposed for bond fracture simulations and related phase change phenomena in the brittle fracture of homogeneous materials [61,65], fracture mechanics in the $\Delta\mu VT$ ensemble consists of probing all bonds in the system by sampling from an ensemble of equilibrated states at fixed bond rupture potential $\Delta\mu$, volume $V = V_0(1+\lambda)$, and temperature T, with V_0 the initial volume and λ a dilation factor. A Nosé-Hoover thermostat is employed to maintain an average temperature of $T^* = k_B T / \min_{(n)} \epsilon_i^0 = 0.1$ in reduced Lennard-Jones (LJ) units. The time step for the MD runs is set to 0.005τ in LJ reduced units (with unit LJ parameters). Simulations are performed using LAMMPS [66] and simulation images are created with OVITO [67].

The bond rupture potential, $\Delta\mu$, is an auxiliary field which, akin to a radiation source, can switch bonds on or off. Moreover, the bond rupture potential only acts on the bonds in the system and not the mass points (i.e., mass points are not being switched on and off). Practically, the semigrand canonical ensemble enables us to toggle the state of a bond between ON and OFF. This directly gives us a way to probe a large number (ensemble) of states with different broken bond configurations. Over the course of the simulation, a convergent behavior is manifested in the form of a crack that traverses the system (more details in [61,65]). Applied to heterogeneous, n-phase, material systems, each phase $J = A, B, \ldots, n$ is defined by a fixed number of mass points with interactions defined by bond potentials.

A. Bond potentials

The interactions between mass points are determined by ground-state energies, $\mathbf{E^0} = (\epsilon_A^0, \epsilon_B^0, \ldots, \epsilon_n^0)$, and elastic energies, $\mathbf{E}^\lambda = (\epsilon_A^\lambda, \epsilon_B^\lambda, \ldots, \epsilon_n^\lambda)$. Restricting ourselves to two-point interactions, bond potentials (of mean force) are of the form

$$u_J(r_{ij}) = -\epsilon_J^0 + \epsilon_J^\lambda \overline{u}_J^{ij}(r_{ij}), \tag{13}$$

with $\overline{u}_J^{ij}(r_{ij})$ a dimensionless expression of the two-point stretch potential in function of bond length, r_{ij}. In this work we consider harmonic and nonharmonic potentials, which only differ in the expression of the stretch potential expression. That is, for a harmonic potential,

$$\overline{u}_J^{ij}(r_{ij}) = \frac{1}{2}\lambda_{ij}^2; \quad \lambda_{ij} = \frac{r_{ij}}{r_0} - 1, \tag{14}$$

and for a Morse potential,

$$\overline{u}_J^{ij}(r_{ij}) = \frac{1}{2k^2}[1 - \exp(-k\lambda_{ij})]^2; \quad k = \sqrt{\frac{\epsilon^\lambda}{2\epsilon^0}}, \tag{15}$$

where r_0 is the distance at equilibrium, for which $\overline{u}_J^{ij}(r_0) = 0$. The chosen parameters of the Morse potential are such that the Morse potential degenerates into the same harmonic potential, given in Eq. (14), around the equilibrium position, $r_{ij} \to r_0$.

For given prescribed values of $\Delta\mu$, V, and T, we evaluate the total energy from the sum over all intact bonds $N = N_0 - N_{br}$, where N_0 is the initial number of bonds, and N_{br} is the number of broken bonds:

$$U = \sum_{k=1}^{N} u_k; \quad U^0 = -\sum_{k=1}^{N} \epsilon_k^0; \quad U^\lambda = \sum_{k=1}^{N} (\epsilon^\lambda \overline{u}^{ij}(r_{ij}))_k, \tag{16}$$

where the energy, $U = U^0 + U^\lambda$, is the sum of ground-state U^0 and stretching U^λ energies over all intact bonds. Broken bonds have zero energy.

B. Application to fracture simulations of heterogeneous model materials

For the investigation of a number of model heterogeneous materials, we carry out bond fracture in SGCMC simulations recently proposed for bond fracture simulations and related phase change phenomena in the brittle fracture of homogeneous materials (for details, see [61,65]).

For SGCMC simulations of the 2D and 3D model materials, we consider the following:

(1) A 2D triangular lattice of dimensions 72×42 squared lattice units, with 6048 mass points and 18,144 bonds;

(2) A 3D $10 \times 10 \times 10$ fcc lattice, with 4000 mass points and 24,000 bonds, for the random geometry;

(3) A 3D $12 \times 12 \times 12$ fcc lattice, with 6192 mass points and 41,472 bonds, for the checkerboard geometry.

Each bond is assigned a ground-state and an elastic energy, the distribution of which is defined by (i) the investigated texture (see Fig. 1) and the volume fraction ($\sim$ bond fraction) of each phase.

While the SGCMC approach permits investigating the entire phase diagram of brittle fracture [61], we are interested in this investigation only in the "effective" fracture resistance in uniaxial tension. Hence, in our simulations we set $\Delta\mu = 0$ and increase the volume $V = V_0(1+\lambda)$ until we reach the critical "Griffith" state defined by Eq. (6), for which (i) $\lambda = \lambda^{\mathrm{crit}} \leftrightarrow q^0 \equiv -q^\lambda$, and for which (ii) we observe a first-order phase transition (for a discussion, see [61,65]).

To simulate a uniaxial deformation at an angle θ inclined to the simulation box coordinates X, Y, Z, we make use of standard tensor projections:

$$\lambda = \vec{n} \cdot \varepsilon \cdot \vec{n}; \quad \varepsilon = \varepsilon_{ij} \vec{e}_i \otimes \vec{e}_j, \tag{17}$$

where $\vec{n}$ is the direction of stretch application, whereas ε is the strain tensor in the X, Y, Z components of ε_{ij}. For instance, a uniaxial tensile dilation in the (X, Y) plane in the $\theta = \pi/4$ direction (see Fig. 2) corresponds to a combined biaxial tension and shear loading, with $\varepsilon_{xx} = \varepsilon_{yy} = \varepsilon_{xy} = \lambda/2$.

IV. RESULTS

We proceed by exploring bond fracture correlations and dependence for a number of geometrically ordered and disordered two-phase, $n = 2$ model composites (Fig. 1), defined by different ground-state and stretch energies, ϵ_J^0 and ϵ_J^λ, respectively, for phases $J = A, B$. With a focus on the "effective" ground-state energy of the two-phase composite, we evaluate the right-hand side of the fluctuation-based fracture criterion Eq. (6), considering $U^0 = U_A^0 + U_B^0$ and $N = N_A + N_B$ with $U_J^0 = -\epsilon_J^0 N_J$:

$$q^0 = \epsilon_A^0 \frac{\sigma_{N_A}^2}{\sigma_N^2} + \epsilon_B^0 \frac{\sigma_{N_B}^2}{\sigma_N^2} + \left(\epsilon_A^0 + \epsilon_B^0\right) \frac{\mathrm{Cov}(N_A, N_B)}{\sigma_N^2}. \tag{18}$$

Recognizing $\sigma_N^2 = \sigma_{N_A}^2 + \sigma_{N_B}^2 + 2\mathrm{Cov}(N_A, N_B)$, we obtain the effective ground-state energy release of the composite as

$$q^0 = \epsilon_A^0 + \left(\epsilon_B^0 - \epsilon_A^0\right) S_\beta, \tag{19}$$

with S_β the bond fraction (of B phase bonds) participating in bond fracture:

$$S_\beta = \frac{\mathrm{Cov}(N_B, N)}{\sigma_N^2} = \frac{1}{2}\left(1 - \frac{\sigma_{N_A}^2 - \sigma_{N_B}^2}{\sigma_N^2}\right). \tag{20}$$

That is, Eqs. (19) and (20) define a fluctuation-based homogenization criterion of the "effective" ground-state energy from the sole knowledge of the bond variances of the involved phases, $\sigma_{N_A}^2 = \mathrm{Cov}(N_A, N_A)$ and $\sigma_{N_B}^2 = \mathrm{Cov}(N_B, N_B)$, and the total bonds, $\sigma_N^2 = \mathrm{Cov}(N, N)$. These bond variances are assessed by means of SGCMC simulations recently proposed for bond fracture simulations and related phase change phenomena in the brittle fracture of homogeneous materials [61,65].

We choose a set of 2D triangular and 3D fcc lattices on which to perform SGCMC simulations. From converged Monte Carlo simulations, we extract the random variables, N_A, N_B. We determine bond number fluctuations of the two phases, $\sigma_{N_A}^2$ and $\sigma_{N_B}^2$, and the total bond number fluctuation, σ_N^2, and obtain from Eq. (8) the participating bond fractions, $S_\beta = 1 - S_\alpha$.

A. Layered material and the equiprobable Hill bound

The first case we consider is a two-phase layered material uniaxially strained in the θ-direction [Fig. 1(a)]. Akin to the Voigt-Reuss bounds in elasticity, the layered system stretched parallel ($\theta = 0$) and orthogonal ($\theta = \pi/2$) to the layer direction are the simplest geometric representations of uncorrelatedness and independence, which define the upper and lower bounds, respectively. The results shown in Figs. 2(a) and 2(b), as a function of f_B and θ, confirm the relevance of the upper and lower bounds in Eq. (9) and show a convergence of $S_\beta(\theta)$ to the Hill bound for $0 < \theta \to \pi/4$. At $\theta = \pi/4$, the bond fraction follows the Hill bound up to $f_B = 1/2$, beyond which $S_\beta = 0$ [Fig. 2(a)]. The convergence to the Hill bound is marked by the absence of any data points between the Hill bound and the lower bound. Results shown in Fig. 2 are obtained with harmonic potentials of constant ground-state energy, $\kappa_0 = \epsilon_B^0/\epsilon_A^0 = 2$, and elastic energy, $\kappa_\lambda = \epsilon_B^\lambda/\epsilon_A^\lambda = 2$, ratios. Keeping the energy potential formulation constant, the change in effective fracture resistance is exclusively in function of volume fraction f_B and loading orientation angle θ.

Analysis of the probability definition of S_β from Eq. (12) provides further insights for the range of the participant volume fraction between the upper and lower bounds. Given f_B and θ, the conditional probability $P(\beta \mid f_B, \theta)$ of a bond in the B phase to be activated by the load direction is

$$P(\beta \mid f_B, \theta) = \vec{e}_f \cdot \vec{n} = \cos\theta, \tag{21}$$

where $\vec{e}_f$ is the layer orientation, and $\vec{n}$ the stretch direction. In return, since the volume fraction f_B and the angle of load application θ are independent, the joint probability is $P(f_B \cap \theta) = P(f_B)P(\theta) = f_B \cos\theta$. Moreover, considering the Radon–Nikodym theorem, the joint probability of β and (f_B, θ) is obtained when noting

$$P(\beta \mid f_B, \theta) = \frac{dP(\beta \cap f_B, \theta)}{dP(f_B, \theta)}, \tag{22}$$

that is,

$$P(\beta \cap f_B, \theta) = \int_{(f_B,\theta)} P(\beta \mid f_B, \theta) dP(f_B, \theta). \tag{23}$$

Further denoting that $dP(f_B, \theta) = \cos(\theta) df_B - f_B \sin(\theta) d\theta$, we obtain, after integration,

$$P(\beta \cap f_B, \theta) = \frac{f_B}{2}(3\cos^2\theta - 1) \geqslant 0. \tag{24}$$

Finally, considering the fracture processes in the two phases as independent ($P(\beta \cap f_A, \theta) = 0$), the bond fraction is obtained:

$$S_\beta = P(\beta) = P(\beta \cap f_B, \theta) \geqslant 0. \tag{25}$$

An evaluation of the joint probability provides $S_\beta(f_B, \theta) = (f_B/2)(3\cos^2\theta - 1)$ and defines a range of loading angles $\theta \in [0, \arctan(\sqrt{2}) \approx 54.74^\circ]$, in which the reinforcing phase contributes to the "effective" fracture resistance of the composite [Fig. 2(b)]. Moreover, when constrained to the Hill bound [i.e., $S_\beta(f_B, \theta) \geqslant S_\beta^{\mathrm{Hill}} = f_B/2$], a critical state line, $f_B^{\mathrm{crit}} - \theta^{\mathrm{crit}}$ [inset of Fig. 2(b)], is obtained:

$$0 \leqslant f_B^{\mathrm{crit}} = 3\cos^2\theta^{\mathrm{crit}} - 1 \leqslant 1, \tag{26}$$

which separates—in uniaxial tension—cooperative interactions [Fig. 2(c)] from exclusive interactions [Fig. 2(d)] between the two phases. Exclusive interactions are defined by the lower bound, once the equiprobability of bond fracture is exhausted [Fig. 2(e)].

From SGCMC simulations we find (i) that the fracture processes in the two phases are almost uncorrelated [i.e., $\mathrm{Cov}(N_A, N_B) = 0$], and (ii) that $S_\beta = 0$ as soon as the layered system has exhausted the equiprobable Hill bound for all f_B and θ.

More insight can be gained about $S_\beta \to 0$ in Fig. 2(b) by plotting it in a different set of axes, namely, $\sqrt{f_B - S_\beta}$ vs

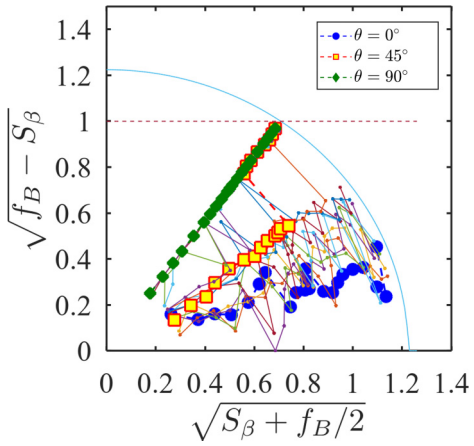

FIG. 3. Geometric representation of the range of loading angles for layered materials for which $S_\beta > 0$. The red dashed line represents the maximum value of the $\sqrt{f_B - S_\beta}$ axis (= 1). The radius of the blue quarter circle is the maximum of the $\sqrt{S_\beta + \frac{f_B}{2}}$ axis ($= \sqrt{\frac{3}{2}}$). All lines with $S_\beta = 0$ collapse on to the line of slope $\tan\theta^* = \sqrt{2}$. Direction of increasing θ is counterclockwise.

$\sqrt{S_\beta + \frac{f_\beta}{2}}$. This set of axes follows directly from the triangle whose cosine satisfies Eq. (24). In Fig. 3 the slopes of the lines are defined by $\tan\theta^*$, where θ^* is the effective loading angle as opposed to the actual loading angle θ. The red dashed line sets the maximum allowable slope as it is the plot of $\max\sqrt{f_B - S_\beta} = 1$, where $S_\beta = 0$ and $S_\alpha = 1$ reaches its maximum value,[1] whereas the minimum allowed slope is the x axis corresponding to the plot of $\min\sqrt{f_B - S_\beta} = 0$. The min-max values of $0 \leqslant \sqrt{f_B - S_\beta} \leqslant 1$ correspond to the upper and lower bounds of fracture resistance, respectively.

It is worth noting that the angle $\theta_m \approx 54.74°$, where $S_\beta \to 0$, is also associated with zero strain lines and necking in ductility of sheet metal [68–70] and zero force in assemblies of magnets, and is even termed magic-angle spinning in NMR spectroscopy [71,72]. This broad scope of null behavior suggests a geometric interpretation for θ_m. Consider a loading vector of magnitude $\sqrt{S_\beta + \frac{f_B}{2}}$, as a function of the fracture resistance and volume fraction, and a fiber orientation vector for a layered material with magnitude $\sqrt{f_B + \frac{f_B}{2}}$, solely as a function of the volume fraction. Define the angle between them as θ^*. Then the difference between the loading and fiber orientation vectors is a vector with magnitude $\sqrt{f_B - S_\beta}$, and we retrieve the same triangle defined by Eq. (24) and axes plotted in Fig. 3.

B. Random material: Elasticity-mediated activation of long-range, collective interactions

The second case considered is a two-phase material with randomly assigned binary ground-state and elastic bond energies, $(\epsilon_A^0, \epsilon_A^\lambda)$ or $(\epsilon_B^0, \epsilon_B^\lambda)$ [Fig. 1(c)], which is most likely

[1] $\max\sqrt{f_B - S_\beta} = \max\sqrt{1 - S_\beta} = \max\sqrt{S_\alpha} = \max S_\alpha = 1$, where $S_\alpha + S_\beta = 1$ for a two-phase material.

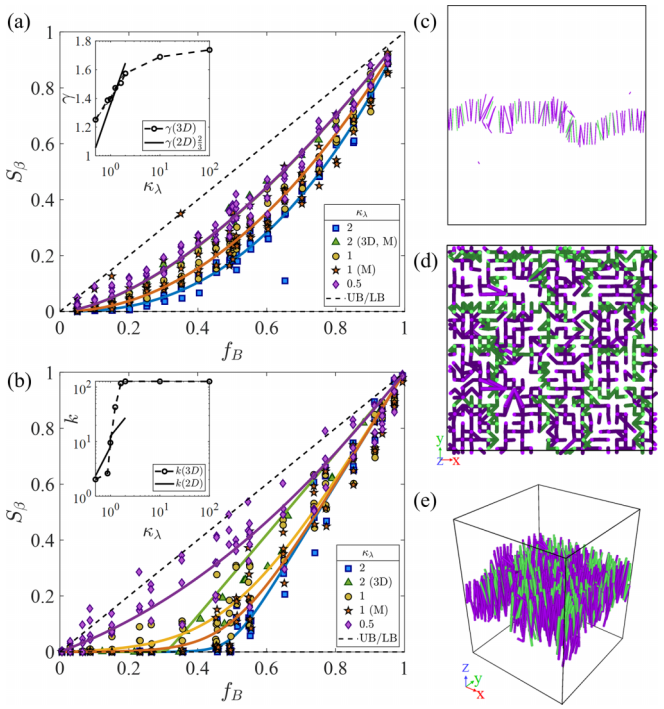

FIG. 4. Elastic toughening in fracture of two-phase (a, c) random and (b, d, e) textured model composites subject to uniaxial stretching in the semigrand canonical ensemble: (a, b) bond fraction, $S_\beta(f_B) \sim f_B^\gamma$, contributing to "effective" bond fracture energy, $q^0 = \epsilon_A^0 + (\epsilon_B^0 - \epsilon_A^0)S_\beta$. Inset (a): exponent γ vs elastic energy mismatch, $\kappa_\lambda = \epsilon_B^\lambda/\epsilon_A^\lambda$. Inset (b): percolation correlation factor k vs κ_λ. Fracture images shown for $f_B = 50\%$ (c) 2D and (d, e) 3D geometries. [SGCMC results obtained with harmonic and Morse potentials (M) of ground-state energy ratio $\kappa_0 = \epsilon_B^0/\epsilon_A^0 = 2$.] Markers are simulation results and solid lines are one-parameter fits using (a) γ [Eq. (28)] and (b) k [Eq. (B4)].

the simplest, i.e., analytically tractable, system among random lattice models [35–37]. In fact, SGCMC simulations show that the bond fraction scales as $S_\beta^{3/d} = f_B^\gamma$, where the dimension correction $3/d$ accounts for the difference in sampling volume between 2D and 3D. The exponent $\gamma \in [1, 2]$ is mediated only by the elasticity mismatch between the two phases, $\kappa_\lambda = \epsilon_B^\lambda/\epsilon_A^\lambda$. This is shown in the inset of Fig. 4(a), from which we conclude that the exponent approaches the lower bound, $\gamma = 1$, for low values of the elastic mismatch ratio, $\kappa_\lambda = \epsilon_B^\lambda/\epsilon_A^\lambda < 1$, and approaches asymptotically $\gamma = 2$ for high values of κ_λ.

Our starting point for the analysis of the random geometry is a probability estimate of bond fracture. Akin to weighted coin flipping, the conditional probability of a binary system is

$$P(\beta \mid f_B) = f_B, \tag{27}$$

where the joint and total probability according to Eqs. (8) and (12) are

$$S_\beta = P(\beta) = P(\beta \mid f_B)P(f_B) = f_B^2, \tag{28}$$

that is, $\gamma = 2$. This probability estimate ignores bond interactions. Insight into these interactions is provided by the two-point correlation function (see Sec. A 2), applied to the

broken bonds of the two phases (i.e., $J = \alpha, \beta$) for different volume fractions and elastic mismatch ratios.

Two-point correlation functions have been widely demonstrated in the literature to be effective descriptors of material heterogeneity, relating the geometric distribution of materials to their properties [56,57,73,74]. Typical examples of two-point correlation functions for the two phases $[S_2^\alpha(r), S_2^\beta(r)]$, together with the cross correlation $(S_2^{(\alpha,\beta)})$, are shown in Fig. 5(a). Moreover, we verify that the value of $S_2^\beta(r)$ respects the asymptotes of two-point correlation functions [73], that is,

$$\forall f_B; \quad S_2^\beta(r=0) = S_\beta; \quad S_2^\beta(r\to\infty) = S_\beta^2. \tag{29}$$

This is shown in Fig. 5(b), where we plot $S_2^\beta(r=0)$ vs $S_\beta = \mathrm{Cov}(N_B, N)/\sigma_N^2$ [from Eq. (20)].

A second important piece of information provided by the two-point correlation function is the mean chord length of broken bonds ℓ_c^β, expressed in a dimensionless form [74]:

$$\left.\frac{dS_2^\beta}{d(r/r_c)}\right|_{r\to 0} = -\frac{S_2^\beta(0)}{(\ell_c^\beta/r_c)}, \tag{30}$$

where r_c^B is the potential cut-off radius [see Eqs. (13) and (14)]:

$$r_c^B = r_0\left(1+\sqrt{2\frac{\epsilon_B^0}{\epsilon_B^\lambda}}\right) = r_0\left[1+\left(1-\frac{r_c^A}{r_0}\right)\sqrt{\frac{\kappa_0}{\kappa_\lambda}}\right]. \tag{31}$$

Figure 5(c) displays the normalized mean chord length ℓ_c^β/r_c^B as a function of the volume fraction f_B. It is remarkable to note that the normalized mean chord length ℓ_c/r_c^B collapses onto a single master curve $\mathcal{S}_0'$ for all f_B and all mismatch ratios κ_λ, that is,

$$\forall f_B, \forall \kappa_\lambda, \quad \frac{\ell_c^\beta}{r_c^B} = \mathcal{S}_0'(f_B), \tag{32}$$

where $\mathcal{S}_0'(f_\beta)$ [displayed in Fig. 5(c)] has asymptotes $\mathcal{S}_0'(f_\beta = 0) = 0$ and $\mathcal{S}_0'(f_\beta = 1) \to \infty$.

At large values of $\kappa_\lambda \gg 1$, the conditional probability can be estimated to be $P(\beta \mid f_B) = f_B$, for which reason $S_\beta = P(\beta \mid f_B)P(f_B) = f_B^2$, recovering Eqs. (27) and (28). For small elastic mismatch, $\kappa_\lambda < 1$, insight is provided by the mean chord length ℓ_c^i, measured from slope of the two-point correlation function over the fracture surfaces at $r \to 0$ [see Eq. (30) and inset of Fig. 5(a)].

We find that the mean chord length scales linearly with the cut-off radius, r_c^J, $\ell_c^B/r_0 \propto r_c^B/r_0 = 1 + (1 - r_c^A/r_0)\sqrt{\kappa_0/\kappa_\lambda}$, for all volume fractions and mismatch ratios $\kappa_0 = \epsilon_B^0/\epsilon_A^0$ and $\kappa_\lambda = \epsilon_B^\lambda/\epsilon_A^\lambda$ and r_0, the equilibrium bond length. The mean chord length of the broken bonds thus holds the key to understanding the elastic toughening mechanism of random bimaterials: for large values of κ_λ, for which $\lim_{\kappa_\lambda\gg 1}(\ell_c^B/r_0) = 1$, the bond fracture is dominated by short-range interactions defined by the lattice size r_0, and hence $\gamma = 2$ [inset of Fig. 4(a)]. In return, as the elastic mismatch is inversed, so that the tougher phase (B) is more compliant than the weaker phase (A), the mean chord length of fracture bonds increases, $\ell_c^\beta/r_0 \propto \kappa_\lambda^{-1/2}$, reminiscent of long-range, collective interactions, approaching the upper bound $\gamma = 1$.

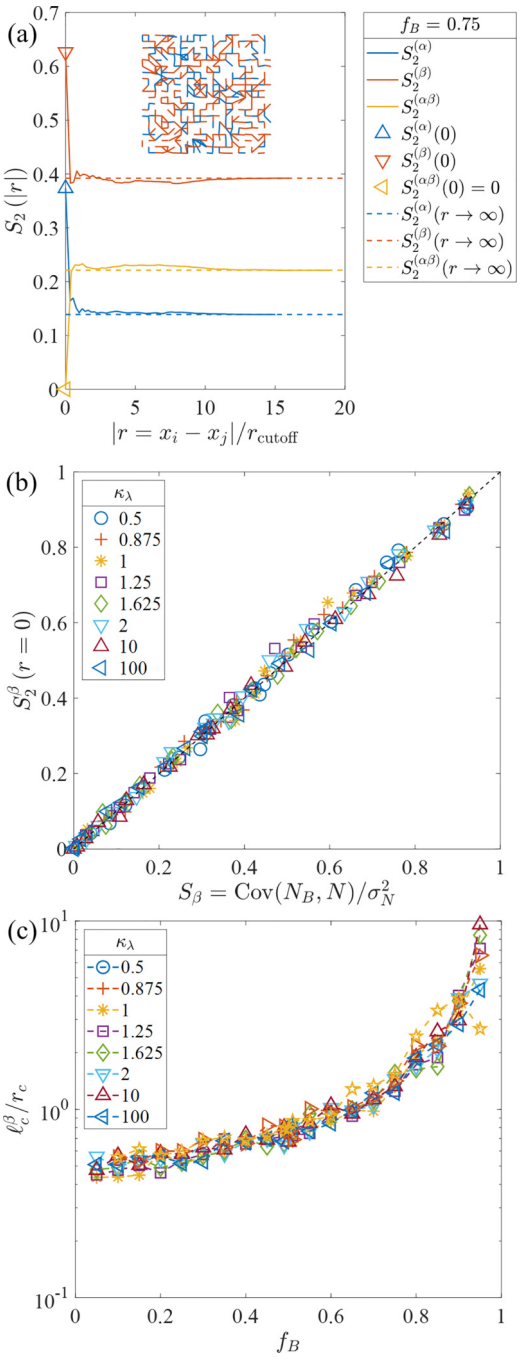

FIG. 5. Two-point correlation function S_2^β of broken bonds for random binary two-phase material: (a) example of 2-pt correlation function $S_2^\alpha(r)$, $S_2^\beta(r)$, $S_2^{(\alpha,\beta)}(r)$ for $f_B = 0.75$. Inset displays broken bonds of the two phases projected on fracture plane orthogonal to load direction. (b) Cross-plot of $S_2^\beta(r=0)$ obtained from single realizations vs S_β obtained from bond fluctuations of the (entire) equilibrated semigrand canonical ensemble at different elastic mismatch ratio, $\kappa_\lambda = \epsilon_B^\lambda/\epsilon_A^\lambda$. (c) Normalized mean chord length of broken bonds ℓ_c^β/r_c^B vs volume fraction f_B ($r_c^B = r_{\mathrm{cutoff}}$ is the potential cut-off radius).

C. Textured material: Elasticity-induced softening of percolation

Moreover, this soft-tough paradigm is not restricted to random materials but manifests itself for highly textured materials as well. For illustration, consider the prototype of a two-phase textured material: a 2D checkerboard [Fig. 1(b1)] and a 3D "checkercube" constructed in a simple cubic (sc) fashion by adjacent cubes of different ground-state and elastic bond energy [Fig. 1(b2)]. In contrast to layered and random materials, textured materials may exhibit a percolation threshold p_c for the activation of the reinforcing phase, i.e., a critical probability of phase B to be part of an infinite cluster (i.e., the macrocrack).

We start from probability considerations, assuming that bond fracture exhibits a similar *hard* site percolation. This is captured by a step-function conditional probability,

$$P(\beta \mid f_B) = \frac{H(f_B - p_c)}{\int_0^1 H(f_B - p_c) df_B}, \tag{33}$$

where $H(x)$ is the Heaviside function. After integrating Eq. (33), we obtain an estimate of the probability of bond fracture for *hard* site percolation, for $\kappa_\lambda \gg 1$:

$$S_\beta = \int P(\beta \mid f_B) dP(f_B) = \frac{|f_\beta - p_c|}{1 - p_c}. \tag{34}$$

A comparison with SGCMC results readily shows that site percolation dominates the composite response for large κ_λ values but fails to capture the bond fraction at small elastic mismatch values, $\kappa_\lambda < 1$ [see Fig. 4(b)].

Proceeding as before, an insight is provided by the two-point correlation of the *broken* bonds of each phase [inset of Fig. 6(a)]. In fact, as shown in Fig. 7, the chord lengths for different volume fractions exhibit Dirac-delta -type behavior at the site percolation threshold p_c. We herein address how this site percolation affects the bond fracture of the textured system.

We verify that the two-point correlation function for each phase at $r = 0$ provides an estimate of the participating bond fraction, $S_2^\alpha(r = 0) = S_\alpha$ and $S_2^\beta(r = 0) = S_\beta$ [see Fig. 6(a)]. This allows us to inspect the mean chord length of the broken bonds for both phases following Eq. (30). The results are displayed in Figs. 6(b) and 6(c). The following observations deserve attention: (i) For large values of elastic mismatch, $\kappa_\lambda = \epsilon_B^\lambda/\epsilon_A^\lambda > 1$, the mean chord length of the weaker phase, ℓ_c^α (broken A bonds) diverges at the geometric site percolation threshold $f_\beta = p_c$, at which point the weaker phase (A) becomes part of a continuous (i.e., infinite) cluster of broken A bonds (α), as one expects from a site percolation phenomenon [Fig. 7(a)]. (ii) As the elastic mismatch is reduced and inverted ($\kappa_\lambda < 1$), the divergence disappears—a hallmark of a smooth phase transition. In other words, a more compliant B phase deactivates bond fracture in phase A (α), in favor of bond fracture in phase B (β). (iii) The mean chord length of broken B bonds ℓ_c^β remains (almost) continuous, shifting from a constant value below the percolation threshold to a monotonically increasing value above, determined by texture. More specifically, below percolation, $f_B < p_c$, the mean chord length scales with the cut-off radius, $\ell_c^\beta \sim r_c^B$ [see Eq. (31)] until it reaches the mean chord length, which characterizes the texture, defined by $\ell_c^\beta \sim f_B^2(1 - f_B)^{(1/d)-1}$, considering the specific surface, $s \sim f_B/\ell_c$, of the B phase beyond percolation in the checkerboard ($d = 2$) or checkercube ($d = 3$).

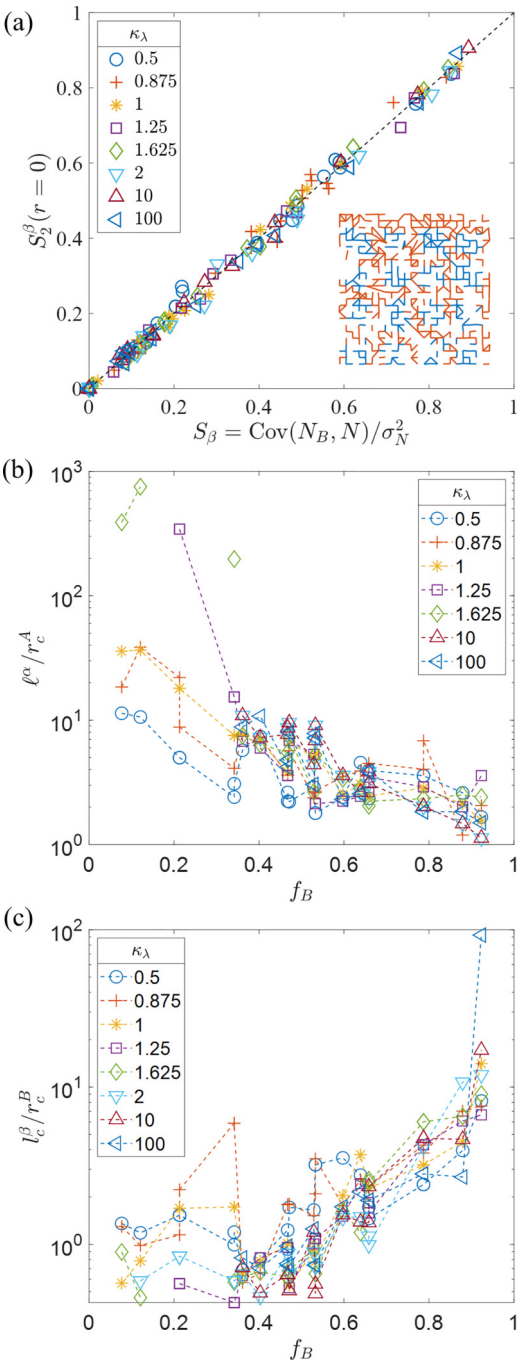

FIG. 6. Two-point correlation function and mean chord length of broken bonds for two-phase checkercube composite: (a) Cross-plot of $S_2^\beta(r = 0)$ obtained from single realizations vs S_β obtained from bond fluctuations of the (entire) equilibrated semigrand canonical ensemble at different elastic mismatch ratio, $\kappa_\lambda = \epsilon_B^\lambda/\epsilon_A^\lambda$. Inset displays broken bonds of the two phases projected on fracture plane orthogonal to load direction for $f_B = 0.787$. (b, c) Normalized mean chord length of broken bonds: (b) ℓ_c^α/r_c^A and (c) ℓ_c^β/r_c^B vs volume fraction f_B (r_c^A and r_c^B are potential cut-off radius of phase A and B).

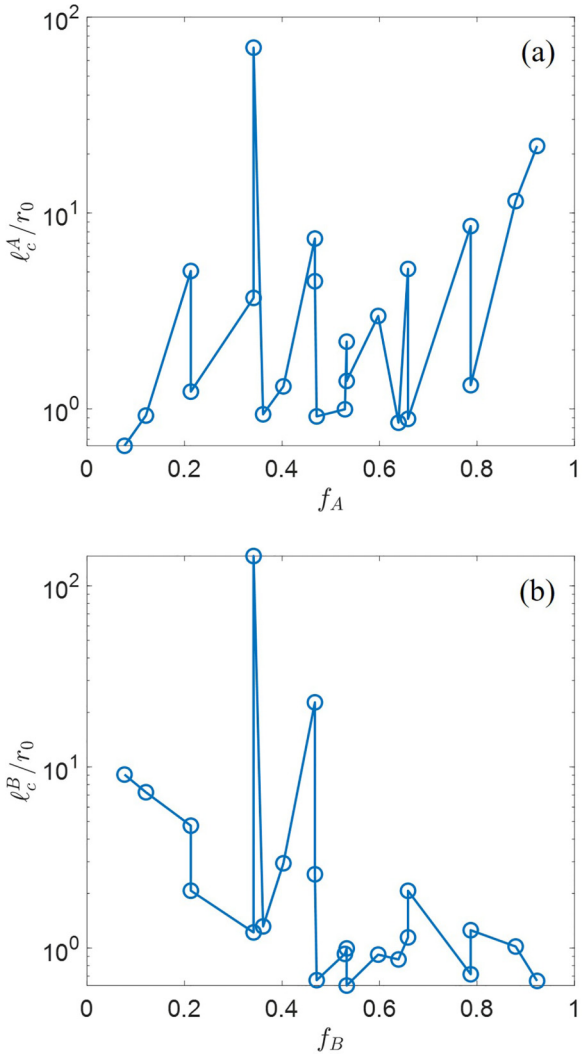

FIG. 7. Mean chord length of 3D checkercube vs volume fraction for (a) phase A, ℓ_c^A/r_0 vs f_A, and (b) phase B, ℓ_c^B/r_0 vs f_B, obtained from the two-point correlation function, $S_2^J(r)$ $(J = A, B)$, of intact lattice bonds (r_0 is lattice distance).

It is thus not surprising that we find the site percolation threshold reproduced in the fracture bond activation for large values of elasticity contrast $\kappa_\lambda \gg 1$, namely, the square-lattice percolation threshold $p_c = 1/2$ for the 2D checkerboard, and the simple cubic percolation threshold $p_c = 0.31$ for the checkercube [Fig. 4(b)]. Table I provides a summary highlighting key parameters of the cases considered in this study so far.

TABLE I. List of parameters and probability formulations for the layered, random, and checkerboard geometries with the corresponding equations in which they appear.

Geometry	$P[\beta\|f_B,\cdot]$	Eq.
Layered θ	$\cos\theta$	(21)
Random γ	$f_B^{\gamma-1}$	(27), (28)
Checkerboard p_c	$\frac{H(f_B-p_c)}{\int_0^1 H(f_B-p_c)df_B}$	(33)

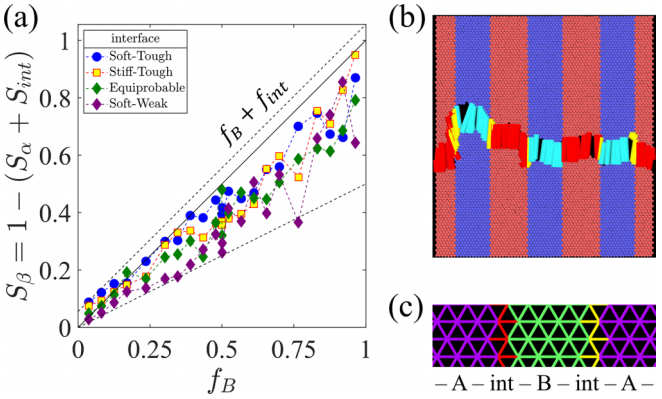

FIG. 8. Elastic toughening due to interfaces of two-phase layered material: (a) bond fraction of reinforcing phase $S_\beta(f_B)$ contributing to "effective" bond fracture energy $q^0 = \epsilon_A^0 + (\epsilon_B^0 - \epsilon_A^0)S_\beta + (\epsilon_{\rm int}^0 - \epsilon_A^0)S_{\rm int}$, with upper, lower, and Hill bound of two-phase material; (b) bond fracture pattern in uniaxial stretching with (c) interface bonds as a separate phase. SGCMC results obtained with harmonic potentials.

D. Role of interfaces

A last point of inquiry we address here is the role of interfaces on the probability of bond fracture. All results so far obtained consider two-phase *equiprobable* interface conditions, i.e., alternating interface properties, which exclude weak or strong bonding at interfaces, that have been suggested as cause of fiber pull-out and delamination of inclusions in, e.g., ceramic matrix composites [75,76]. An explicit account of interface behavior requires consideration of a three-phase material to estimate from Eq. (8) the bond volume fractions of bulk and interface phases $[\mathbf{S} = (S_\alpha, S_\beta, S_{\rm int})^T$ for $S_\alpha + S_\beta + S_{\rm int} = 1]$ with interface properties $(\epsilon_{\rm int}^0, \epsilon_{\rm int}^\lambda)$ that differ from the bulk phase properties [Fig. 8(c)]. For illustration, we investigate for the layered system the impact of interface conditions (Fig. 8). While tough interfaces $(\epsilon_{\rm int}^0 > \epsilon_A^0)$ increase the "effective" bond fracture energy according to Eq. (8) within the equiprobable Hill bound of the two-phase material and the upper bound of the three-phase material, $f_\beta/2 \leqslant S_\beta \leqslant f_\beta + f_{\rm int}$, we find yet another example of the soft-tough paradigm in composite materials when the tough interface bonds are simultaneously compliant [Fig. 8(a)].

V. CONCLUSION

In summary, we have shown that SGCMC simulations provide a means to rationalize the complexity of fracture of heterogeneous materials, from random to highly textured materials, encompassing probability and percolation theories of fracture within a unified framework of fluctuation-based fracture mechanics. In the semigrand canonical ensemble, bond-energy fluctuations permit identifying theoretical upper and lower bounds of fracture resistance, which are critical to ascertain the toughening mechanism in composite materials, such as the soft-tough paradigm induced by elastic mismatch between phases. At low elastic contrast, toughening can result from a shift from short- to long-range interactions of bond fracture processes in random systems, the softening of sharp site percolation thresholds in textured materials, or the

activation of toughness reserves at compliant interfaces. While counterintuitive at first sight, this soft-tough paradigm can be connected to a number of experimental observations, ranging from toughening of brittle solids by highly deformable polymers or organics, such as gas shale (brittle clay minerals reinforced by soft kerogen) [77] or nacre (brittle bricks of aragonite glued together by thin biofilms at interfaces) [78], to stress-induced transformational toughening mechanisms in ceramics [79,80], and toughening of sparse elastic networks relevant for, e.g., hydrogels [81]. For such specific applications, the model composites considered in this work merit refinements to account for realistic texture and interactions beyond the two-point harmonic and Morse potentials considered here, including the three- and four-point bending interactions required for the application of the SGCMC methodology to fracture more complex molecular, mesoscale, and beam- and plate-type engineering structures [82–84]. Finally, given the link between SGCMC simulations and statistical descriptors of heterogeneity such as two-point correlation functions, an important step beyond this work consists in extending the SGCMC approach of bond fracture sampling to experimental sampling of fracture morphology and roughness [40–44] to measure the effective fracture toughness of heterogeneous materials. While this paper is theoretical and simulation-based, independent verification of the results and ideas of this paper exist in the literature [58] [compare with insets of Figs. 4(d), 5(a), and 6(a)], leaving open avenues for future experimental work that will be based on the fluctuation-based fracture mechanics approach presented here. Furthermore, experimental methods in the literature have shown success in describing fracture of heterogeneous material by creating boundary conditions that allow for following the crack tip, as we follow the bonds in our simulations [25,29,85]. Future work will also be able to explicitly define the ground-state energy of materials as a material property proportional to the fracture energy. Exciting extensions of this work would expand the binary choice of MC moves (ON to OFF and OFF to ON) to be able to model progressive damage before ultimate bond failure; future work will also focus on nonbonded interactions to envelope a larger domain of failure models.

ACKNOWLEDGMENT

Research carried out by the Concrete Sustainability Hub (CSHub@MIT), with funding provided by the Portland Cement Association (PCA) and the Ready Mixed Concrete Research & Education Foundation (RMC E&F). We are grateful for discussions with and advice of Professor Mehran Kardar and Professor David M. Parks at MIT.

APPENDIX A: EQUIVALENT MEASURES OF BOND FRACTION S_β IN THE SEMIGRAND CANONICAL ENSEMBLE

The determination of the bond fraction S_β from SGCMC simulations is based on the outcome of converged SGCMC simulations; that is, a large number of—say MC—realizations for which the probability of bond insertion is equal to the probability of bond deletion (i.e., Eqs. (2) and (3), respectively). Restricting ourselves to two-phase materials, we denote by N_A^j, N_B^j, and N^j, for $j = 1, \ldots, MC$, the corresponding bond numbers in these realizations and their broken complements, $N_{A,br}^j = N_{A,0}^j - N_A^j = N_\alpha^j$, $N_{B,br}^j = N_\beta^j$, and $N_{br}^j = N_0 - N^j$, respectively.

The reference measure is the fluctuation-based definition [Eq. (20)]. It can be viewed as a linear regression of (N_B^j, N_j):

$$\widehat{N_B}^j = \overline{N_B} + S_\beta(N^j - \overline{N}) \tag{A1}$$

with

$$S_\beta = \frac{\partial \widehat{N_B}^j}{\partial(N^j - \overline{N})} = \frac{\mathrm{Cov}(N_B, N)}{\sigma_N^2} \tag{A2}$$

where $\overline{N_B}$ and $\overline{N}$ respectively stand for the mean of N_B^j and N^j. By definition, the same holds for the broken bonds when letting $\widehat{N_\beta}^j = N_{B,0} - \widehat{N_B}^j$:

$$\widehat{N_\beta}^j = \overline{N_\beta} + S_\beta\left(N_{br}^j - \overline{N_{br}}\right), \tag{A3}$$

with

$$S_\beta = \frac{\partial \widehat{N_\beta}^j}{\partial(N_{br}^j - \overline{N_{br}})} = \frac{\mathrm{Cov}(N_\beta, N_{br})}{\sigma_{N_{br}}^2}. \tag{A4}$$

Then let $e^j = N_\beta^j - \widehat{N_\beta}^j$ be the residuals between the realization N_β^j and the linear regression $\widehat{N_\beta}^j$ of zero mean ($\overline{e} = 0$). Furthermore, let $N_\beta^j = S_\beta^j N_{br}^j$ and $\overline{N_\beta} = \overline{S_\beta^j N_{br}^j}$, and hence

$$\widehat{N_\beta}^j = S_\beta N_{br}^j + \overline{\left(S_\beta^j - S_\beta\right)N_{br}^j}. \tag{A5}$$

If we remind ourselves of the dual definition Eq. (11), which implies $\overline{N_\beta} = S_\beta \overline{N_{br}}$, the second term in Eq. (A5) is zero, while $e^j / N_{br}^j = S_\beta^j - S^\beta$. A single realization j out of an equilibrated semigrand canonical ensemble thus provides a first-order estimate of the bond fraction:

$$\forall j; \quad S_\beta^j = S_\beta + \frac{e^j}{N_{br}^j}. \tag{A6}$$

A cross-plot of $S_\beta^j = N_\beta^j / N_{br}^j$ vs $S_\beta = \mathrm{Cov}(N_B, N)/\sigma_N^2$ allows one to ascertain relevance of the first-order approximation $S_\beta \approx S_\beta^j$, shown in Fig. 9.

1. Bond fraction of broken bonds

Equation (7) suggests yet another definition of S_β from the second mixed derivative of the ground-state energy. To this end, we express the effective heat of bond rupture due to ground-state energy in terms of covariances; that is, for the two-phase material,

$$q^0 = -\frac{d\langle U^0\rangle}{d\langle N\rangle} = -\frac{\mathrm{Cov}(U^0, N)}{\sigma_N^2} = \epsilon_A^0 S_\alpha + \epsilon_B^0 S_\beta. \tag{A7}$$

It is thus recognized that

$$S_\beta(f_B) = -\left.\frac{d^2\langle U^0\rangle}{d\epsilon_B^0 d\langle N\rangle}\right|_{f_B} = \left.\frac{d\langle N_B\rangle}{d\langle N\rangle}\right|_{f_B} = \text{constant}. \tag{A8}$$

After integration with the initial condition $N_B(N = N_0) = N_{B,0} = f_B N_0$, we obtain

$$N_B = N_{B,0} - S_\beta(N_0 - N), \tag{A9}$$

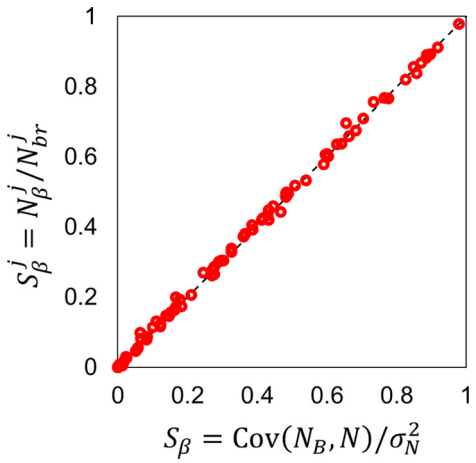

FIG. 9. Cross-plot of $S_\beta^j = N_\beta^j/N_{br}^j$ vs $S_\beta = \mathrm{Cov}(N_B, N)/\sigma_N^2$. The dashed line is the line $S_\beta^j = S_\beta$, showing S_β^j is a good first-order approximation of S_β.

which finally leads to

$$S_\beta(f_B) = \frac{N_{B,0} - N_B}{N_0 - N} = \frac{N_\beta}{N_{br}}, \tag{A10}$$

where $N_{br} = N_0 - N$ and $N_\beta = N_{B,0} - N_B$ are the broken number of bonds in the system and broken bonds of phase B, respectively. S_β is thus defined as the volume (bond) fraction of broken bonds, in agreement with Eq. (11) and all simulation results (see Fig. 9).

This view of the participant volume fractions readily extends to multiphase materials:

$$N_J = N_{J,0} - \left.\frac{dN_J}{dN}\right|_{f_J} (N_0 - N). \tag{A11}$$

Equation (A11) is a Taylor expansion of N_J around N_0 (up to the first derivative), reinforcing the fact that fracture requires a small amount (<10%) of broken bonds to generate a macrocrack across the entire system.

2. Link with two-point correlation function of broken bonds

In this work we show that S_β^j can also be determined from the two-point correlation function of broken bonds of a realization j, thus proposing a direct link between theory and practice:

$$S_\beta^j = S_2^\beta(r = 0) = \sqrt{S_2^\beta(r \to \infty)}. \tag{A12}$$

As a reminder, the two-point correlation function for a phase J is defined by [56,57]

$$S_2^J(r = ||\vec{r}_2 - \vec{r}_1||) = \langle I^J(\vec{r}_1) I^J(\vec{r}_2)\rangle, \tag{A13}$$

where $I^J(\vec{r}_i)$ is the indicator function of phase J:

$$I^J(\vec{r}_i) = \begin{cases} 1 & \text{if} \quad i \in J \\ 0 & \text{if} \quad i \notin J \end{cases}. \tag{A14}$$

The second important information provided by the two-point correlation function is the mean chord length, ℓ_c:

$$\left.\frac{dS_2^J}{dr}\right|_{r\to 0} = -\frac{S_2^J(0)}{\ell_c}. \tag{A15}$$

The mean chord length is close to a multiplying function equal to the specific surface [73]. Therefore, for a homogeneous material ($f_J = 1$), for which $S_2(r) = 1$, the slope is zero and hence $\ell_c \to \infty$; in the dilute limit of $f_J \ll 1$, the slope is infinite and hence $\ell_c \to 0$.

APPENDIX B: CRITICALITY OF PERCOLATION THRESHOLD IN CHECKERBOARD GEOMETRY IN 2D AND 3D

We confirm the criticality of percolation in the form of the divergence of the mean chord length of broken bonds in the weaker phase, ℓ_c^α (broken A bonds) at the geometric site percolation threshold $f_B = p_c$. The chosen textured model materials have known geometric site percolation thresholds at $p_c = 0.5$ for the 2D square lattice and $p_c = 0.31$ for the 3D simple cubic lattice [see Figs. 1(b1) and 1(b2)]. The site percolation thresholds are readily obtained from the mean chord length derived from the two-point correlation functions of the lattice bonds of the two phases of volume fraction $S_2^A(0) = f_A$ and $S_2^B(0) = f_B$:

$$\left.\frac{dS_2^A}{dr}\right|_{r\to 0} = -\frac{f_A}{\ell_c^A}; \quad \left.\frac{dS_2^B}{dr}\right|_{r\to 0} = -\frac{f_B}{\ell_c^B}. \tag{B1}$$

When the elastic mismatch is reduced and inversed ($\kappa_\lambda < 1$), the divergence disappears—a hallmark of a smooth phase transition associated with a change from critical to subcritical percolation behavior. To capture this transition, we introduce a smoothed step function, $H^* = (1 + \exp[-k(f_B - p_c)])^{-1}$, with $k \sim \ell_c$ the only adjustable parameter to fit the simulation results. As shown in Fig. 4(b), the elastic toughening mechanism in textured materials results from a transition from a hard step-function (critical) percolation probability at high κ_λ values where $k \gg 1$ to a subcritical percolation at low κ_λ values where $k = O(1)$ [inset Fig. 4(b)], while S_β approaches the upper bound [Fig. 4(b)].

In summary, the comparative analysis of the mean chord length of intact and broken bonds shows that the elastic toughening of the considered textured materials is due to the smoothing of the hard percolation of the weaker phase (A) at the geometric percolation threshold of the tougher phase (B). To capture this transition in terms of the participating bond fraction, we consider a smooth approximation of the Heaviside function:

$$H^*(f_B - p_c) = \frac{1}{1 + \exp[-k(f_B - p_c)]}, \tag{B2}$$

where the regularization factor k permits transitioning from the step function ($k \to \infty$) to a smooth transition, in terms of the conditional probability:

$$P(\beta \mid f_B) = \frac{H^*(f_B - p_c)}{\int_0^1 H^*(f_B - p_c) df_B}. \tag{B3}$$

We thus obtain

$$S_\beta(f_B) = \frac{\ln(1+e^{-k(f_B-p_c)}) - \ln(1+e^{kp_c}) + kf_B}{\ln(1+e^{-k(1-p_c)}) - \ln(1+e^{kp_c}) + k}. \quad \text{(B4)}$$

Using Eq. (B4) to fit the simulation results, we obtain k in function of the elastic mismatch ratio [inset of Fig. 4(b)], showing that the regularization factor k diverges for large values of κ_λ, which mimics the mean chord length of the weaker phase.

[1] C. K. H. Dharan, J. Eng. Mater. Technol. **100**, 233 (1978).
[2] G. Bao, S. Ho, Z. Suo, and B. Fan, Int. J. Solids Struct. **29**, 1105 (1992).
[3] G. Constantinides, K. R. Chandran, F.-J. Ulm, and K. Van Vliet, Mater. Sci. Eng., A **430**, 189 (2006).
[4] K. Sieradzki and R. Li, Phys. Rev. Lett. **56**, 2509 (1986).
[5] H. Laubie, F. Radjai, R. Pellenq, and F.-J. Ulm, Phys. Rev. Lett. **119**, 075501 (2017).
[6] S. L. Kramer, A. Jones, A. Mostafa, B. Ravaji, T. Tancogne-Dejean, C. C. Roth, M. G. Bandpay, K. Pack, J. T. Foster, M. Behzadinasab *et al.*, Int. J. Fract. **218**, 5 (2019).
[7] E. A. Papon and A. Haque, Addit. Manuf. **26**, 41 (2019).
[8] Z. Jia and L. Wang, Acta Mater. **173**, 61 (2019).
[9] S. Kamat, X. Su, R. Ballarini, and A. Heuer, Nature (London) **405**, 1036 (2000).
[10] H. Gao, Int. J. Fract. **138**, 101 (2006).
[11] H. Yao, Z. Xie, C. He, and M. Dao, Sci. Rep. **5**, 8011 (2015).
[12] H.-C. Loh, T. Divoux, B. Gludovatz, P. Gilbert, R. Ritchie, F.-J. Ulm, and A. Masic, Commun. Mater. **1**, 77 (2020).
[13] A. Griffith, Philos. Trans. R. Soc. London, Ser. A **221**, 163 (1921).
[14] E. Orowan, Rep. Prog. Phys. **12**, 185 (1949).
[15] G. R. Irwin and J. A. Kies, Welding Journal **33**, 193s (1954).
[16] G. Irwin, J. Appl. Mech. **24**, 361 (1957).
[17] A. G. Evans and K. T. Faber, J. Am. Ceram. Soc. **64**, 394 (1981).
[18] H. Gao and J. R. Rice, J. Appl. Mech. **56**, 828 (1989).
[19] M. Mower and A. Argon, Mech. Mater. **19**, 343 (1995).
[20] A. F. Bower and M. Ortiz, J. Mech. Phys. Solids **39**, 815 (1991).
[21] K. T. Faber and A. G. Evans, Acta Metall. **31**, 565 (1983).
[22] M.-Y. He and J. Hutchinson, Int. J. Solids Struct. **25**, 1053 (1989).
[23] D. K. Shum and J. W. Hutchinson, Mech. Mater. **9**, 83 (1990).
[24] Y. Shao, H.-P. Zhao, X.-Q. Feng, and H. Gao, J. Mech. Phys. Solids **60**, 1400 (2012).
[25] M. Hossain, C.-J. Hsueh, B. Bourdin, and K. Bhattacharya, J. Mech. Phys. Solids **71**, 15 (2014).
[26] H. Laubie, F. Radjai, R. Pellenq, and F.-J. Ulm, J. Mech. Phys. Solids **105**, 116 (2017).
[27] S. Yi, S. Gao, and L. Shen, Int. J. Solids Struct. **38**, 4463 (2001).
[28] J. Ma, M.-S. Mo, X.-S. Du, P. Rosso, K. Friedrich, and H.-C. Kuan, Polymer **49**, 3510 (2008).
[29] N. R. Brodnik, C.-J. Hsueh, K. T. Faber, B. Bourdin, G. Ravichandran, and K. Bhattacharya, J. Appl. Mech. **87**, 031018 (2020).
[30] N. R. Brodnik, S. Brach, C. M. Long, G. Ravichandran, B. Bourdin, K. T. Faber, and K. Bhattacharya, Phys. Rev. Lett. **126**, 025503 (2021).
[31] E. Castillo, *Extreme Value Theory in Engineering*, Statistical Modeling and Decision Science (Elsevier Science, New York, 2012).
[32] S. Biswas, P. Ray, and B. K. Chakrabarti, *Statistical Physics of Fracture, Breakdown, and Earthquake: Effects of Disorder and Heterogeneity* (John Wiley & Sons, New York, 2015).
[33] Z. P. Bažant and J.-L. Le, *Probabilistic Mechanics of Quasibrittle Structures: Strength, Lifetime, and Size Effect* (Cambridge University Press, Cambridge, England, 2017).
[34] Z. P. Bažant and S.-D. Pang, J. Mech. Phys. Solids **55**, 91 (2007).
[35] P. D. Beale and D. J. Srolovitz, Phys. Rev. B **37**, 5500 (1988).
[36] A. Delaplace, G. Pijaudier-Cabot, and S. Roux, J. Mech. Phys. Solids **44**, 99 (1996).
[37] M. J. Alava, P. K. Nukala, and S. Zapperi, Adv. Phys. **55**, 349 (2006).
[38] Z. Bertalan, A. Shekhawat, J. P. Sethna, and S. Zapperi, Phys. Rev. Appl. **2**, 034008 (2014).
[39] S. Biswas, L. Goehring, and B. K. Chakrabarti, Philos. Trans. R. Soc., Ser. A **377**, 20180202 (2019).
[40] J. Schmittbuhl, S. Gentier, and S. Roux, Geophys. Res. Lett. **20**, 639 (1993).
[41] J. Schmittbuhl, F. Schmitt, and C. Scholz, J. Geophys. Res.: Solid Earth **100**, 5953 (1995).
[42] D. Sornette, Phys. Rep. **297**, 239 (1998).
[43] E. Bouchaud, Surf. Rev. Lett. **10**, 797 (2003).
[44] S. Zapperi, P. K. V. Nukala, and S. Šimunović, Phys. Rev. E **71**, 026106 (2005).
[45] S. Roux, A. Hansen, and E. Guyon, J. Phys. **48**, 2125 (1987).
[46] M. Sahimi, *Heterogeneous Materials I: Linear Transport and Optical Properties*, Vol. 22 (Springer Science & Business Media, New York, 2003).
[47] W.-Z. Cai, S.-T. Tu, and J.-M. Gong, J. Compos. Mater. **40**, 2131 (2006).
[48] C. Bowen and D. P. Almond, Mater. Sci. Technol. **22**, 719 (2006).
[49] I. S. Aranson, V. A. Kalatsky, and V. M. Vinokur, Phys. Rev. Lett. **85**, 118 (2000).
[50] R. Spatschek, E. Brener, and A. Karma, Philos. Mag. **91**, 75 (2011).
[51] D. Bonamy and E. Bouchaud, Phys. Rep. **498**, 1 (2011).
[52] J. Chopin, A. Bhaskar, A. Jog, and L. Ponson, Phys. Rev. Lett. **121**, 235501 (2018).
[53] M. Lebihain, L. Ponson, D. Kondo, and J.-B. Leblond, J. Mech. Phys. Solids **153**, 104463 (2021).
[54] V. Démery, A. Rosso, and L. Ponson, EPL (Europhys. Lett.) **105**, 34003 (2014).
[55] V. Démery, V. Lecomte, and A. Rosso, J. Stat. Mech.: Theory Exp. (2014) P03009.
[56] S. Torquato, J. Beasley, and Y. Chiew, J. Chem. Phys. **88**, 6540 (1988).
[57] S. Torquato, Appl. Mech. Rev. **44**, 37 (1991).
[58] Y. Barak, A. Srivastava, and S. Osovski, Int. J. Fract. **219**, 19 (2019).
[59] S. Roux, D. Vandembroucq, and F. Hild, Eur. J. Mech. A. Solids **22**, 743 (2003).

[60] T. L. Anderson, *Fracture Mechanics: Fundamentals and Applications* (CRC Press, Boca Raton, FL, 2017).
[61] T. Mulla, S. Moeini, K. Ioannidou, R. J.-M. Pellenq, and F.-J. Ulm, Phys. Rev. E **103**, 013003 (2021).
[62] R. J.-M. Pellenq and P. E. Levitz, Mol. Phys. **100**, 2059 (2002).
[63] W. Nicholson, D. Nicholson, and N. G. Parsonage, *Computer Simulation and the Statistical Mechanics of Adsorption* (Academic Press, New York, 1982).
[64] T. Al-Mulla, R. J.-M. Pellenq, and F.-J. Ulm, Eng. Fract. Mech. **199**, 544 (2018).
[65] T. Mulla Mahmoud, Sc.D. thesis, Massachusetts Institute of Technology, 2021.
[66] S. Plimpton, J. Comput. Phys. **117**, 1 (1995).
[67] A. Stukowski, Modell. Simul. Mater. Sci. Eng. **18**, 015012 (2010).
[68] A. Nádai, *Theory of Flow and Fracture of Solids*, Engineering Societies Monographs (McGraw-Hill, New York, 1950), Vol. 1.
[69] R. Hill, *The Mathematical Theory of Plasticity*, Vol. 11 (Oxford University Press, Oxford, England, 1998).
[70] C. Li, E. Daxin, and N. Yi, J. Mater. Res. **31**, 3991 (2016).
[71] M. J. Duer, *Solid State NMR Spectroscopy: Principles and Applications* (John Wiley & Sons, New York, 2002).
[72] M. Salehizadeh and E. Diller, Int. J. Rob. Res. **39**, 1377 (2020).
[73] P. Smith and S. Torquato, J. Comput. Phys. **76**, 176 (1988).
[74] H. Laubie, S. Monfared, F. Radjai, R. Pellenq, and F.-J. Ulm, J. Mech. Phys. Solids **106**, 207 (2017).
[75] R. W. Rice, in Proceedings of the 9th Annual Conference on Composites and Advanced Ceramic Materials: Ceramic Engineering and Science Proceedings (John Wiley & Sons, Ltd., New York, 1985), Chap. 11, pp. 589–607.
[76] K. Konopka, M. Maj, and K. J. Kurzydłowski, Mater. Charact. **51**, 335 (2003).
[77] P. Kabir, F.-J. Ulm, and A.-T. Akono, Acta Geotech. **12**, 1207 (2017).
[78] H. Kakisawa and T. Sumitomo, Sci. Tech. Adv. Mater. **12**, 064710 (2011).
[79] A. Evans and A. Heuer, J. Am. Ceram. Soc. **63**, 241 (1980).
[80] H. Pan and G. Weng, Acta Mech. **156**, 47 (2002).
[81] T. Yamaguchi, Y. Onoue, and Y. Sawae, Phys. Rev. Lett. **124**, 068002 (2020).
[82] M. Bauchy, Mohammad Javad Abdolhosseini Qomi, C. Bichara, F.-J. Ulm, and Roland J.-M. Pellenq, Phys. Rev. Lett. **114**, 125502 (2015).
[83] K. Keremides, M. J. A. Qomi, R. J.-M. Pellenq, and F.-J. Ulm, J. Eng. Mech. **144**, 04018066 (2018).
[84] A. Morshedifard, M. Ruiz-García, M. J. A. Qomi, and A. Košmrlj, J. Mech. Phys. Solids **149**, 104296 (2021).
[85] C.-J. Hsueh, G. Ravichandran, and K. Bhattacharya, in *Fracture, Fatigue, Failure and Damage Evolution* (Springer, New York, 2016), Vol. 8, pp. 151–155.